Nonlinear response of graphene to a few-cycle terahertz laser pulse: Role of doping and disorder

Larisa A. Chizhova, Florian Libisch,* and Joachim Burgdörfer
Institute for Theoretical Physics, Vienna University of Technology (TUW), Wiedner Hauptstraße 8-10, 1040 Vienna, Austria, EU
(Received 29 March 2016; published 9 August 2016)

The nonlinear response of graphene to a THz laser pulse is studied by solving the time-dependent Dirac equation and the time-dependent Schrödinger equation within a tight-binding approximation applied to finite-sized structures. We compare predictions of these two approximations for the harmonic spectrum with the recent experiment by P. Bowlan *et al.* [Phys. Rev. B **89**, 041408(R) (2014)]. We highlight the influence of short-range and long-range disorder which can be accounted for within the tight-binding description on a microscopic level. We find good agreement with the experiment. Most notably, the intensity of the second harmonic offers a quantitative indicator for the amount of short-range disorder.

DOI: 10.1103/PhysRevB.94.075412

I. INTRODUCTION

Investigation of the nonlinear response of condensed matter to ultrashort few-cycle near-infrared laser pulses has become one key topic in the field of ultrafast optical science [1–7]. Applications to nanostructures, surfaces, and solids hold the promise that nonlinear effects such as high-harmonic generation or directed emission of electrons [8] well known for atomic and molecular targets are strongly enhanced for targets at solid-state densities. Moreover, the response may allow for all-optical probes of the electronic band structure [9,10] or demagnetization at ultrashort time scales [11,12].

A tantalizing extension represents the response of two-dimensional solids. Graphene, a novel 2D material, is also expected to respond nonlinearly to driving by a strong laser field [Fig. 1(a)]. Because of the much smaller energy scales, in particular for the gap between valence and conduction bands, the frequency of the driving field is in the terahertz (THz) rather than the near-infrared region. The nonlinearity in graphene is closely linked to the near-linear dispersion of electrons or holes close to the Dirac point [13] (see Fig. 2). With the advances in THz laser technology achieved in the last years, experimental studies of different nonlinear effects in graphene became feasible, for example, second-harmonic generation [14,15], photon drag effect [16], four-wave mixing [15], as well as the study of nonlinear carrier dynamics [17] and THz generation [18]. The nonlinear low odd harmonic generation in graphene was first studied experimentally by Paul *et al.* [19]. Both an epitaxially grown multilayer (∼20 layers) graphene structure and a single graphene layer produced by chemical vapor deposition (CVD) were investigated but no harmonic generation by strong terahertz fields could be unambiguously detected. However, more recently, Bowlan *et al.* [20] observed for a ∼45 layer graphene sheet odd harmonics in response to short THz pulses with 40 kV/cm field strength and 2 THz frequency. The power spectrum of the detected far-field THz response showed the first, third, and fifth harmonics with relative strengths of 1, 3×10^{-3}, and 5×10^{-4} and, moreover, traces of second-harmonic generation (SHG).

Theoretically, the optical response in the THz regime was investigated by solving the Boltzmann equation [21], the time-dependent Dirac equation [22], and optical Bloch equations [23,24]. In the present paper, we aim for a microscopic quantum-mechanical simulation of the electron dynamics which allows for a quantitative treatment of short-range scatterers (e.g., lattice defects) and long-range disorder. We solve the time-dependent Schrödinger equation of an electron in a finite-size graphene flake subject to a time-dependent pulse by third-nearest-neighbor time-dependent tight-binding (TDTB). We benchmark our approach against simulations of pristine bulk graphene based on the time-dependent Dirac equation (TDDE), and find qualitative and, overall, quantitative agreement. The TDTB approach allows for inclusion of different types of disorder, superlattice potentials due to the substrate (for example, hBN [25]) as well as imperfections of the band structure such as trigonal warping and electron-hole asymmetry [26]. We analyze the influence of doping and disorder and find good agreement with the experiment [20]. In particular, our method reproduces the observed traces of SHG when short-range disorder is included, allowing for a quantitative assessment of short-range scatterers from the harmonic spectrum.

II. METHODS

In this paper we apply two alternative methods to calculate the nonlinear response of graphene to a few-cycle THz laser pulse by solving (i) the time-dependent Dirac equation (TDDE) and (ii) the time-dependent Schrödinger equation for graphene within the time-dependent tight-binding (TDTB) approximation. Note that both methods fully account for the nonlinear response of the charge carriers to the electromagnetic field to all orders, and thus implicitly include field-induced renormalization effects of the band structure [27].

The TDDE provides a good approximation of bulk graphene and is very useful for a qualitative understanding of the response. The Dirac equation, however, cannot easily account for disorder and the resulting K-K' scattering. The advantage of the tight-binding method is the opportunity to account for disorder or substrate interactions on a microscopic level. Both

*florian.libisch@tuwien.ac.at

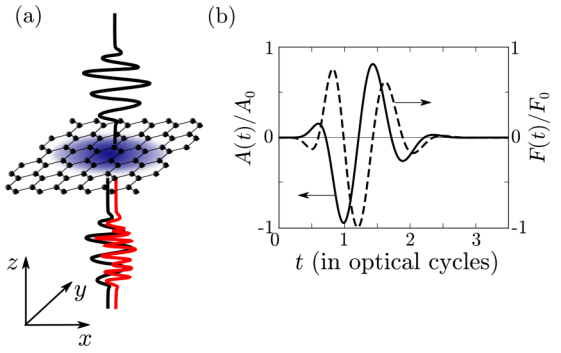

FIG. 1. (a) Nonlinear response in graphene. Schematically, the incoming few-cycle THz laser pulse (black curve) accelerates electrons in graphene, which emit radiation (red curve) at higher frequencies. (b) Electric field (black dashed curve) and vector potential (black solid curve) normalized to the field strength of a 2 THz linear polarized laser pulse given by Eq. (1).

methods represent an independent-particle description, i.e., neglect carrier-carrier scattering. A typical time scale of the ultrafast subcycle dynamics we consider is the cycle period of the order of 500 fs. As carrier relaxation by electron-electron scattering happens on a time scale of several hundreds of femtoseconds [28,29], we expect distortion of the harmonic generation by electron-electron scattering to be of minor importance compared to the effects of disorder scattering and doping.

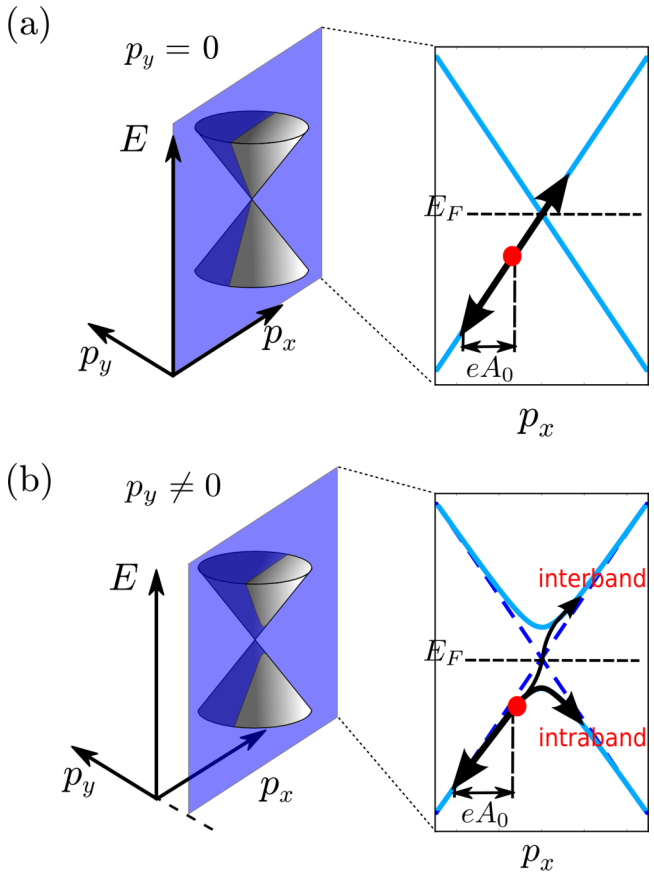

FIG. 2. (a) and (b) Electronic motion on the Dirac cone with different initial momenta: (a) $p_y = 0$; (b) $p_y \neq 0$.

We test our theory for a few-cycle THz pulse linearly polarized along the x axis [Fig. 1(b)]: $A_x(t) \equiv A(t) = A_{\rm env}(t)\sin(2\pi\nu t)$. We model a $\nu = 2$ THz pulse with a period $T = 500$ fs and the envelope

$$A_{\rm env}(t) = A_0 \begin{cases} \exp\left(-\frac{(t-1.1T)^2}{(0.67T)^2}\right), & \text{if } t <= 1.1T; \\ \exp\left(-\frac{(t-1.1T)^{2.7}}{(0.47T)^{2.7}}\right), & \text{otherwise,} \end{cases} \quad (1)$$

where the amplitude of the vector potential $A_0 = F_0/2\pi\nu$ is proportional to the laser field strength F_0. The pulse shape is chosen to resemble the experimental pulse used for observation of nonlinear harmonics [20].

A. Time-dependent Dirac equation

Neglecting the hexagonal lattice structure of graphene reduces the problem to the solution of the TDDE

$$i\hbar\frac{\partial}{\partial t}\Psi(t) = v_F \begin{pmatrix} 0 & pe^{-i\theta_{\vec{p}}} + |e|A(t) \\ pe^{i\theta_{\vec{p}}} + |e|A(t) & 0 \end{pmatrix}\Psi(t), \quad (2)$$

where v_F is the Fermi velocity of Dirac fermions and $\theta_{\vec{p}} = \arctan(p_y/p_x)$ is the directional angle of the momentum of the initial state. Harmonic radiation results from the driven motion of electrons and holes on the Dirac cone (Fig. 2). While nonrelativistic electrons move with velocities following the harmonic oscillations of the laser field, electrons in graphene subject to a laser pulse move on the Dirac cone according to Eq. (2) with velocities exhibiting nonlinear behavior. To illustrate the counterintuitive notion that a near-linear dispersion leads to strong nonlinear effects, let us consider the motion of a relativistic particle driven by a laser pulse linearly polarized in the x direction (Fig. 2). In the case of zero initial momentum in the y direction, i.e., $p_y = 0$, the interband response plays a dominant role as the electron oscillates between the lower and the upper cones [Fig. 2(a)]. Moreover, since the particle moves with constant velocity, there is no acceleration of the charge and, hence, no harmonic generation. If, however, the particle has an initial momentum $p_y \neq 0$ [Fig. 2(b)], its movement is confined to the hyperbola created by an off-center cut through the double cone. Now both movement along one branch of the hyperbola (intraband), as well as quantum tunneling between the two branches (interband) contribute. The strong curvature near the tip of the Dirac cone as well as the induced interband polarization give rise to high-order harmonics.

The numerical solution of the TDDE was discussed in detail by Ishikawa [22,30]. Briefly, Eq. (2) can be solved numerically using the ansatz

$$\Psi(t) = C_+(t)\Psi_+(t) + C_-(t)\Psi_-(t). \quad (3)$$

Here "+" and "−" represent conduction and valence bands, and the wave functions describing states within upper and lower bands have the form

$$\Psi_\pm(t) = \frac{1}{\sqrt{2}}e^{[\mp i\phi(t)]}\begin{pmatrix} e^{-i\theta_{\vec{p}}(t)/2} \\ \pm e^{i\theta_{\vec{p}}(t)/2} \end{pmatrix}, \quad (4)$$

where $\theta_{\vec{p}}(t) = \arctan\{p_y/[p_x + |e|A(t)]\}$ is the directional angle of the canonical momentum and the temporal phase $\phi(t) = v_F \int_0^t \sqrt{[p_x + |e|A(t')]^2 + p_y^2}\, dt'/\hbar$. The single-particle current density induced by the laser field can be evaluated as

$$\vec{j}(t) = \langle\Psi(t)|\hat{\vec{j}}|\Psi(t)\rangle = v_F\langle\Psi(t)|(\sigma_x,\sigma_y)|\Psi(t)\rangle, \quad (5)$$

where $\hat{\vec{j}}$ denotes the current operator and $\sigma_{x,y}$ are the Pauli matrices. The current $\vec{j}(t)$ consists of *intraband* and *interband* contributions. The intraband current created by a particle moving within one band can be analytically expressed as

$$(j_x)^{\text{intra}} = \pm v_F \frac{p_x + |e|A(t)}{\sqrt{[p_x + |e|A(t)]^2 + p_y^2}}. \quad (6)$$

This relation directly follows from the classical equations of motion of a relativistic particle with the dispersion relation

$$E_\pm(t) = \pm v_F \sqrt{\{[p_x + |e|A(t)]^2 + p_y\}} \quad (7)$$

propagating on the lower $[E_-(t)]$ or the upper $[E_+(t)]$ cone [see Figs. 2(a) and 2(b)]. The more complex interband contribution requires a quantum-mechanical description.

The many-electron current is given by the ensemble average over "quantum trajectories," i.e., over an ensemble of solutions of the TDDE or the TDTB equations, expressed in terms of the reduced one-particle density ρ, as

$$\langle\vec{J}(t)\rangle = \sum_n \langle\Psi_n(t)|\hat{\vec{j}}|\Psi_n(t)\rangle P_n, \quad (8)$$

where P_n are the occupation numbers, i.e., the eigenvalues of the reduced one-body density matrix ρ prior to the pulse. In the following $P_n(t \to -\infty)$ is given by the Fermi-Dirac distribution function $f_{\text{FD}}(\epsilon_n - \mu)$ with the chemical potential μ.

It is instructive to analyze the contributions of individual quantum trajectories $|\Psi_n(t)\rangle$, i.e., the solution of the TDDE with the eigenstates of ρ, the natural orbitals, as initial states. In the case of the TDDE the initial state is defined by the initial momentum $(n = \vec{p})$. A valence electron in graphene with an initial momentum $\vec{p} = (p_x,0)$ driven by an external laser field contributes a constant current [22] $\vec{j} = (-v_F,0)$ [red line in Fig. 3(a)], because in this case the massless Dirac electron moves with constant velocity. When the applied ponderomotive momentum $|e|A_0$ exceeds in magnitude the initial momentum, the response is governed by interband dynamics. The valence electron in the lower cone passes through the Dirac point and reaches the conduction band (upper cone). If the electron would remain on the lower cone (i.e., intraband dynamics), the current would change sign [Eq. (6)] at the Dirac point [green curve in Fig. 3(a)]. The windowed Fourier transform (WFT) [31] of the wave function $\Psi(t)$ [Fig. 3(b)] indicates the complete transfer from the lower to the upper cone at the Dirac point, i.e., at $E = 0$, which results in a constant current. The trajectory in energy space smoothly alternates between the two cones [i.e., between red and black dashed curves in Fig. 3(b) corresponding to intraband trajectories].

A fundamentally different situation arises for $p_y \neq 0$. For low-lying initial states in the valence band with energy $|E| =$

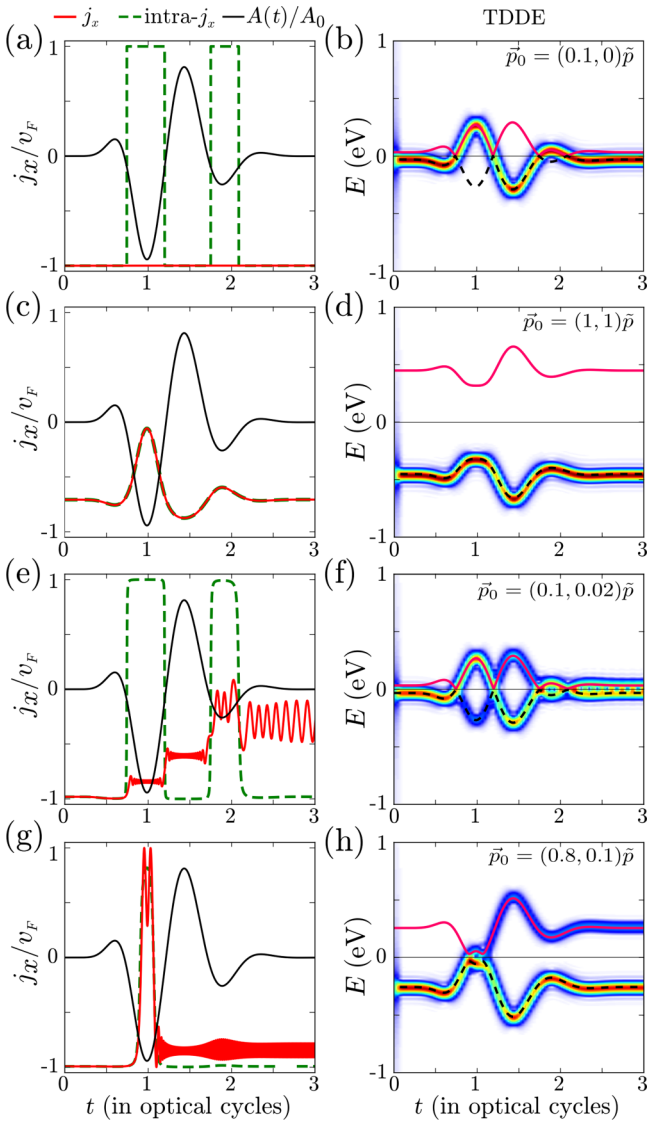

FIG. 3. Left column: Time evolution of total (red solid curves) and intraband (green dashed curves) currents evaluated within the Dirac model using TDDE Eq. (2) and Eq. (6) for individual quantum trajectories $|\Psi_{\vec{p}}(t)\rangle$ corresponding to initial states in the valence band at $t \to -\infty$ with different initial momenta: (a) $\vec{p} = (0.1,0)|e|A_0$; (c) $\vec{p} = (1.0,1.0)|e|A_0$; (e) $\vec{p} = (0.1,0.02)|e|A_0$; (g) $\vec{p} = (0.8,0.1)|e|A_0$. The black solid curve in all plots represents the normalized vector potential of the THz laser pulse. Right column: Windowed Fourier transform of $|\Psi_{\vec{p}}(t)\rangle$ corresponding to the initial conditions of panels (a), (c), (e), and (g) showing the energy evolution of the wave packet (color scale: white-blue-yellow-red). Black dashed and red solid curves correspond to the classical energy evolution $[E_\pm(t)$ in Eq. (7)] for the electron motion in the valence $[E_-(t)]$ and the conduction $[E_+(t)]$ bands, respectively.

$v_F|\vec{p}|$ larger than the maximal energy $v_F|e|A_0$ a particle can gain from the pulse, the dynamics is reduced to the electron motion within the valence band, described by the *intraband* current [Eq. (6)]. The intraband response coincides with the total response [Fig. 3(c)]. Consequently, the energy evolution of the particle [i.e., the WFT of the wave function Fig. 3(d)]

follows the intraband energy evolution within the lower band only [black dashed curve in Fig. 3(d)].

For initial energies $|E_n| \lesssim v_F|e|A_0$ and nonzero p_y, the response features a coherent superposition of interband and intraband dynamics. The total current strongly deviates from the pure intraband current [Figs. 3(e) and 3(g)] and displays strong oscillations. The latter arises from the interband polarization due to electron tunneling between the valence and conduction bands. The strength of this Landau-Zener type tunneling process depends exponentially on the energy gap between the two cones at the $p_y =$ constant conical intersection [see Fig. 2(b)] [32]. Part of the wave packet then propagates on the upper band $E_+(t)$ while the other portion of the wave packet still follows the classical trajectory $E_-(t)$ in the lower band [Figs. 3(f) and 3(h)]. The superposition of two parts of the wave packet results in a beating of current with frequency $2\dot{\phi}(t)$ since the two parts of the wave packet acquire phases of opposite sign $e^{i\phi(t)}$ and $e^{-i\phi(t)}$ while moving on the valence and the conduction cones. The oscillations are time-dependent and their frequency $\Omega(t) = 2\dot{\phi}(t) = [E_+(t) - E_-(t)]/\hbar = 2E(t)/\hbar$ is given by the energy difference between the two pathways. The highest oscillation frequency is realized when the two paths reach their maximal separation in energy. Such oscillations are absent in the pure intraband response [see Figs. 3(e) and 3(g)].

The foregoing description can be extended to the case where, e.g., graphene-substrate interactions lead to a band gap opening E_g at the Dirac point resulting in Dirac fermions with a finite mass m. In this more general case the time-dependent Dirac equation reads

$$i\hbar\frac{\partial}{\partial t}\Psi = v_F\begin{pmatrix} mv_F & pe^{-i\theta_{\vec{p}}} + |e|A(t) \\ pe^{i\theta_{\vec{p}}} + |e|A(t) & -mv_F \end{pmatrix}\Psi. \quad (9)$$

The band gap $E_g = 2mv_F^2$ is, e.g., for graphene on hexagonal boron nitride of the order of 40 meV [33]. The numerical solution of this equation proceeds analogously to the massless TDDE discussed above.

B. Time-dependent tight binding

As an alternative strategy we employ the time-dependent Schrödinger equation using a third-nearest-neighbor tight-binding (TDTB) Hamiltonian for the graphene lattice

$$i\hbar\frac{\partial}{\partial t}\Psi(t) = H_{\mathrm{TB}}\Psi(t) \quad (10)$$

applied to finite-size graphene flakes. We first validate this approximation by confirming that for sufficiently large flake sizes and low-energy excitations close to the Dirac point, the TDDE results for bulk graphene can be reproduced by TDTB. Beyond the TDDE dynamics, TDTB allows for including realistic effects in graphene such as trigonal warping for higher-lying excitations and the presence of disorder due to localized defects or charge puddles on a microscopic level.

We solve the Schrödinger equation [Eq. (10)] numerically using the short iterative Lanczos propagator (SIL) [34]. The laser pulse is included through its vector potential using the Peierls phase factor [35]. This choice corresponds to the coupling to the electromagnetic field in velocity gauge. This gauge preserves the lattice periodicity and has been proven to be advantageous for describing the strong field and high frequency response in atoms, molecules, and solids [36,37]. However, it may lead to divergences in the near-static limit ($\omega \to 0$) of the response [37,38]. For the TDTB approximation applied to a finite-size graphene flake each quantum trajectory corresponds to the evolution of an eigenstate of the flake $\Psi_n(t)$ in a laser field. The single-electron current of the nth eigenstate is then determined by the probability current:

$$j_x^n(t) = -\frac{i\hbar}{2m}\left\{\left(\Psi_n(t)^*\frac{\partial}{\partial t}\Psi_n(t) - \Psi_n(t)\frac{\partial}{\partial t}\Psi_n(t)^*\right)\right\} + \frac{|e|A(t)}{2m}|\Psi_n(t)|^2. \quad (11)$$

We first calculate the eigenstates of a rectangular graphene flake with dimensions $W_x \times W_y = 250 \times 25$ nm^2 with periodic boundary conditions in the x direction, i.e., along the pulse polarization direction. We screen the zigzag edges parallel to the x axis using a Berry-Mondragon potential to suppress edge effects [39]. For each eigenstate with energy ϵ_n we assign a wave number in the x direction k_x^n by evaluating the Fourier transform of the corresponding eigenfunction and searching for the maximal value of k_x. Plotting $\epsilon_n(k_x^n)$ [Fig. 4(a)] closely resembles the band structure of the infinitely extended nanoribbon of width W_y, including the two inequivalent K and K' Dirac cones. The spectrum of the flake features clear signatures of size quantization in the y direction [Fig. 4(a)]. In particular, a band gap of $E_g = 80$ meV emerges. Obviously, unlike the TDDE, where the initial single-electron wave function can have any momentum of the continuous Dirac spectrum, the eigenstates of the flake allow for probing the electron dynamics only at discrete momenta. The size quantization effects can be reduced by increasing the flake size at additional computational cost. Figures 4(c)–4(e) display, on a single-particle current level, the similarities and differences between solutions of the TDTB [top panels in Figs. 4(c)–4(e)] and the TDDE with an identical band gap of $E_g = 80$ meV [bottom panels in Figs. 4(c)–4(e)]. For the initial states $\psi_n(t \to -\infty)$ in the vicinity of the Dirac point [states marked by 1 and 2 in Fig. 4(a)], the laser-induced tunneling between the bands creates an interband polarization, which we observe as high-frequency oscillations in the current [see Figs. 4(c) and 4(d) and traces marked by 1 and 2 in Fig. 4(b)]. For an initial state $\psi_n(t \to -\infty)$ corresponding to an eigenstate of the flake far away from the Dirac point [marked by 3 in Fig. 4(a)], we observe a suppression of the interband response, and the dynamics is governed by the intraband motion [see Fig. 4(e) and trace marked by 3 in Fig. 4(b)]. Overall, the response as calculated by the TDDE and by the TDTB methods resemble each over. Residual differences result primarily from signatures of size-quantization effects for the flake.

III. SIMULATIONS

A. Ideal graphene

The physical observable in the experiment [20] was the far-field response of graphene, which clearly revealed the presence of higher harmonics in the power spectrum. In the far-field approximation the electromagnetic field generated by the moving charges in graphene due to the interaction with

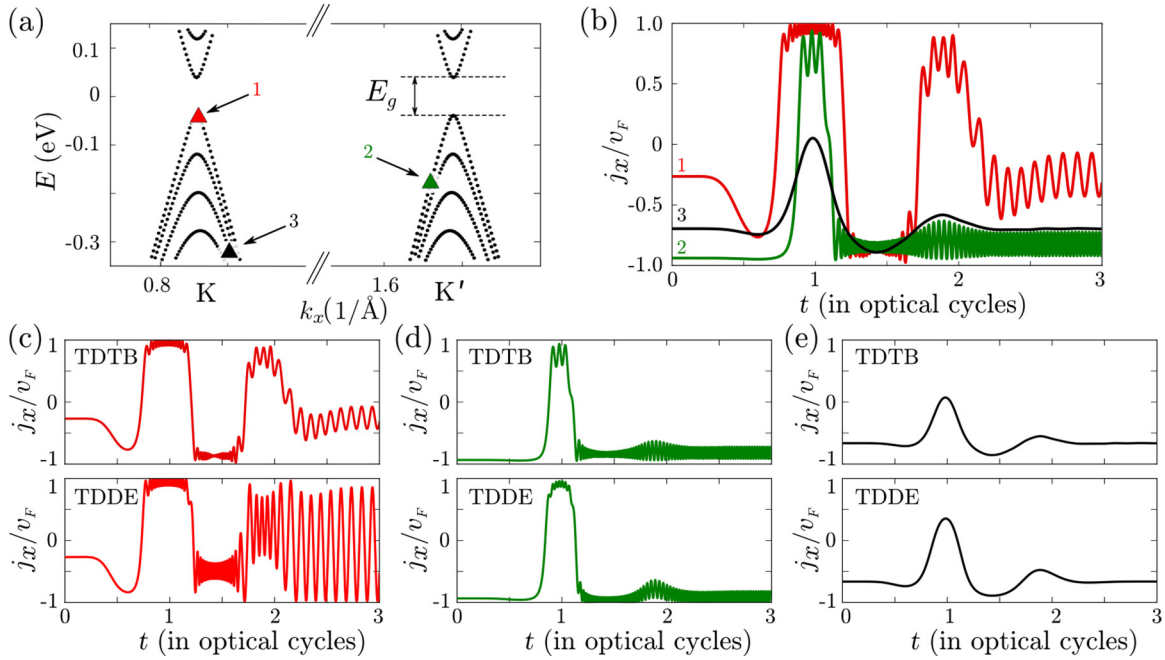

FIG. 4. (a) Spectrum of a $W_x \times W_y = 250 \times 25$ nm^2 flake with periodic boundary conditions in x direction and screened zigzag boundaries parallel to the x axis (blue dots). Red, green, and black triangles (also marked by 1, 2, and 3) denote the initial eigenstates $|\Psi_n\rangle$ for which we show the single-electron current in (b) calculated within TDTB (similarly marked by 1, 2, and 3). (c)–(e) Top panels show the same single-electron currents as in (b) for initial states (1)–(3). Bottom panels display single-electron currents evaluated by solving the TDDE with a finite gap $E_g = 80$ meV for equivalent initial states (1)–(3).

the laser pulse is determined by the dipole acceleration of the charge carriers $\ddot{\vec{d}}(t)$. The squared Fourier transform of the dipole acceleration yields the power spectrum:

$$P(\omega) \propto |\ddot{\vec{d}}(\omega)|^2 = |\omega \dot{\vec{d}}(\omega)|^2. \tag{12}$$

Since both current and first derivative of the dipole moment are proportional to the velocity, we can equivalently write

$$P(\omega) \propto |\omega \langle \vec{J}(\omega) \rangle|^2. \tag{13}$$

Here $\langle \vec{J}(\omega) \rangle$ is a Fourier transform of the total current [30] for an ensemble of occupied initial states

$$\langle \vec{J}_{\mathrm{TDDE}}(t) \rangle = \frac{g_s g_v}{(2\pi\hbar)^2} \int d^2p \, \langle \psi_{\vec{p}}(t) | \hat{\vec{j}} | \psi_{\vec{p}}(t) \rangle \cdot f_{\mathrm{FD}}(v_F |\vec{p}| - \mu), \tag{14a}$$

or

$$\langle \vec{J}_{\mathrm{TDTB}}(t) \rangle = g_s \sum_n \langle \psi_n(t) | \hat{\vec{j}} | \psi_n(t) \rangle \, f_{\mathrm{FD}}(\epsilon_n - \mu), \tag{14b}$$

where $g_s = 2$ and $g_v = 2$ denote spin- and valley-degeneracy. We treat electrons in the valence band with energies $0 \leqslant E \leqslant -0.33$ eV at time $t \to -\infty$ to capture all the states reaching the Dirac point for the pulse strengths we examine. We focus on the far-field response parallel to the polarization axis of the laser; i.e., we evaluate J_x and calculate the power spectrum $P(\omega)$ resulting from this component of the total current. The y component of the current is zero for a symmetric distribution of p_y.

Assuming first an undoped sample with $\mu = 0$, i.e., the Fermi level coincides with the Dirac point, the power spectrum of the graphene response (see Fig. 5) displays the formation of the third and the fifth harmonics with increasing laser intensity starting from a field of $F_0 \approx 20$ kV/cm. Here we have evaluated the total graphene response using four different methods: by solving (i) the TDTB [Eq. (10)] for the finite-sized flake; (ii) the TDDE [Eq. (2)]; (iii) the TDDE with a small band gap of $E_g = 80$ meV [Eq. (9)]; and by evaluating (iv) the intraband response only as given by Eq. (6) within the Dirac model. For strong laser fields ($F_0 = 40$ kV/cm) the power spectrum calculated within the TDDE is very similar to the response due to the intraband current alone. However, at low field strengths ($F_0 = 20$ kV/cm), the solution of the TDDE features stronger nonlinearities due to the additional interband interferences. The results from TDTB closely resemble those of the TDDE, both for a gapless Dirac cone and for massive fermions with a gap chosen to coincide with that of the TDTB simulation ($E_g = 80$ meV). Also the yields for the third and the fifth harmonics [Fig. 5(c)] predicted by the different methods agree with each other. Comparison with the experimental data shows, overall, qualitative agreement while some deviations are noticeable. In particular, the fifth harmonic is clearly underestimated and a second-harmonic component is present in the data but entirely absent in our simulations for an ideal graphene sheet [Fig. 5(c)].

B. Influence of doping and disorder

All the calculations above were performed for zero doping ($\mu = 0$) with occupied states up to the Dirac point. In the experiment, however, finite doping of the sample leads to nonzero μ. The influence of doping on the harmonic intensities can be large. The response near the Dirac point is very sensitive to interband polarizations, which may lower the harmonic intensities. By changing μ these high-frequency

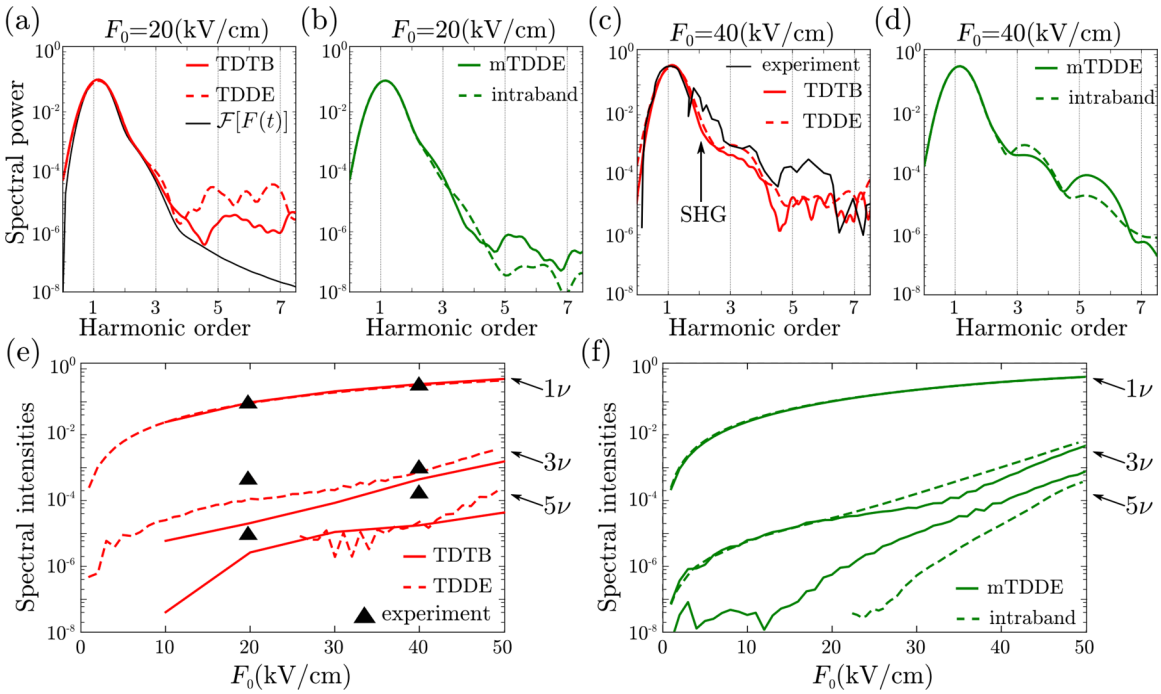

FIG. 5. Power spectrum of the total response of ideal graphene in the absence of doping and disorder at (a), (b) $F_0 = 20$ kV/cm and (c), (d) $F_0 = 40$ kV/cm laser field strengths evaluated with different methods: in (a), (c) TDTB (red solid curves) and TDDE (red dashed curves); in (b), (d) TDDE with a small energy gap $E_g = 80$ meV (green solid curves) and the intraband response (green dashed curves). Each spectrum is normalized to the intensity of the first harmonic in the experiment at the laser field $F_0 = 40$ kV/cm [20]. The black curve in (a) represents the power spectrum of the laser pulse. (e), (f) Spectral intensities of the first (1ν), third (3ν), and fifth (5ν) harmonics as a function of laser field strength evaluated with different methods. Black curve in (c) and black triangles in (e) represent the measured response of graphene [20].

interband-induced oscillations in the current can be reduced and a stronger intraband signal with higher odd harmonics can be observed. The influence of doping was theoretically considered in [21] within the kinetic Boltzmann equation. Al-Naib *et al.* [24] examined the maximization problem of the emitted third harmonic as a function of Fermi energy for the intraband response. Here, we probe the response of graphene within both the TDDE and the TDTB approximations at the experimental field strength of $F_0 = 40$ kV/cm for different values of μ.

A shift of 50 meV in the Fermi level has a dramatic influence on the harmonic spectra of the total current [see Figs. 6(a) and 6(c)]. In particular, we observe an increase of the 5th harmonic by approximately one order of magnitude in both the TDDE and the TDTB, making the harmonic intensity comparable with experiment. This strongly suggests a nonzero doping of the graphene samples used in [20]. Indeed, Bowlan *et al.* [20] estimated a doping level of $\mu = 24$ meV by fitting the measured signal to the Drude model. This doping level, however, leads to a very similar response to that of an undoped graphene in the Dirac picture. The relative magnitudes of the 3rd and 5th harmonics in our calculations agree well with the experiment when a doping of $\mu = 50$ meV is assumed [see Fig. 6(c)].

It should be noted that p- or n-type doping yields similar results: for $\mu > 0$ the occupied states extend to $0 < E \leqslant \mu$ on the upper cone while for $\mu < 0$, the states on the lower cone with $\mu \leqslant E < 0$ are unoccupied. States with the same momentum and the same absolute value of the energy but belonging to upper and lower cones give rise to nearly identical currents with opposite sign (within the Dirac model the currents are exactly opposite) and, therefore, approximately cancel each other. As a result, the current from the energy window $-\mu < E < \mu$ is nearly zero producing a negligible response.

Accounting for a finite temperature up to 300 K by a Fermi-Dirac distribution of undoped graphene smoothens the strong fluctuations in the interband current near the Dirac point. Consequently, the effect of a finite temperature on the response of pristine, undoped graphene is similar to the effect of nonzero doping [Fig. 6(b)] in the TDDE. However, including a finite temperature for a doped sample with $\mu \neq 0$ hardly changes the spectrum or the intensities of low harmonics compared to $T = 0$ [Figs. 6(b) and 6(d)].

The presence of second-harmonic generation (SHG) in the experiment [20] points to an additional effect not accounted for so far. SHG should only appear if inversion symmetry is broken which can be easily included in the TDTB but not in the TDDE simulation. The second-order response to a linearly polarized laser field is

$$j_x^{(2)} \sim \sigma^{(2)} E_x E_x^*, \tag{15}$$

where $\sigma^{(2)}$ is the optical conductivity tensor describing the second-order nonlinearity. This equation describes the so-called linear photogalvanic effect [13,40]. In pristine graphene, i.e., in the absence of local symmetry breaking, the quadratic form $E_x E_x^*$ is invariant under parity transformation, while the current changes its sign. Therefore, the SHG is zero unless

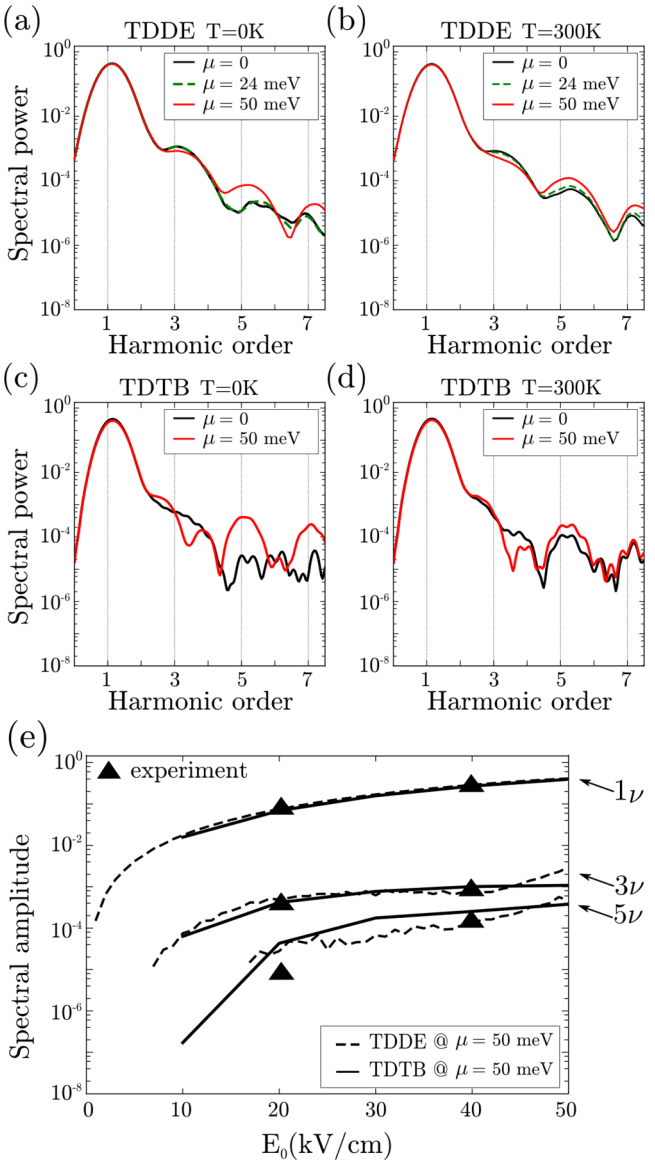

FIG. 6. (a)–(d) Power spectrum of the total response of graphene at different doping levels μ for $F_0 = 40$ kV/cm laser field strength evaluated within (a), (b) the TDDE and (c), (d) the TDTB approximations. Simulations for different temperatures: (a), (c) at $T = 0$ K and (b), (d) at $T = 300$ K. (e) Spectral intensities of the first (1ν), third (3ν), and fifth (5ν) harmonics as a function of laser field strength evaluated with TDDE and TDTB for doping of $\mu = 50$ meV, compared to experiment (triangles, [20]).

the inversion symmetry is broken which leads to increased backscattering of electrons and hence to a portion of the current flowing opposite to the field direction. Major candidates for local symmetry breaking in real crystals are vacancies or adsorbates [41] representing short-range disorder on the length scale of the lattice constant $a_c = 2.46$ Å and charge puddles [42] representing long-range disorder with potential variations extending over distances large compared to a_c.

Disorder is treated by including a disorder potential V_{disorder} as on-site potential into the tight-binding Hamiltonian H_{TB} [Eq. (10)]. The resulting current follows now from an additional ensemble average over different stochastic realizations of the disorder landscape, i.e.,

$$\left\langle \vec{J}^{\text{disorder}}_{\text{TDTB}}(t) \right\rangle = \frac{g_s}{M} \sum_n \sum_{m=1}^{M} \left\langle \Psi_n^{(m)}(t) \middle| \hat{\vec{j}} \middle| \Psi_n^{(m)}(t) \right\rangle P_n, \qquad (16)$$

where $|\Psi_n^{(m)}(t)\rangle$ denotes the quantum trajectory for the mth disorder realization (we consider an ensemble of $M = 5$ realizations) for each initially occupied state n. Such a quantum trajectory Monte Carlo (QTMC) approach [43] allows us to include dephasing by elastic disorder scattering on a microscopic level through appropriate choices of V_{disorder}, eschewing phenomenological scattering time approximations [23,24]. For the present simulations we have neglected electron-electron and electron-phonon scattering in view of the involved time and energy scales: optical phonons with frequencies of the order of 45 THz and energies of ≈200 meV (larger than the electron energies considered here) are expected to be only weakly populated even at 300 K [44]. Acoustic phonons in graphene only weakly couple to electronic transport, resulting in a time scale of a hundred ps, which is much longer than the observed decay times. Consequently, short-range and long-range disorder are expected to dominate over electron-phonon coupling [24]. To first order, quasielastic electron-electron scattering results in the accumulation of random scattering phases, similar to the case of transport in a disordered landscape we consider. Theoretical estimates for electron-electron scattering [45] predict approximately fifty scattering events per picosecond at 1.2 eV, only a fraction of which will be strongly inelastic. Since the electron-electron scattering cross section scales with the density of states—which is lower by an order of magnitude in the energy range we consider—strongly inelastic electron-electron scattering can be neglected for the present pulse duration and pulse strength. Recent work on the dynamic response of multilayer samples finds effective time scales for interlayer coupling of the order of 10–100 ps [46], larger than the pulse duration considered here. Radiative coupling effects [44] should be small due to the small cross section for graphene-photon interactions. As first-order effect we would expect a small decrease in the harmonic response due to destructive interference of the response from different layers. Note that intraband absorption [47] can be neglected in the energy range we consider, as the small energy transfer of a single photon does not require additional phonon coupling to fulfill momentum conservation. The validity of these considerations is further corroborated by the excellent agreement of theory and experiment [Fig. 6(e)]. We note that electron-electron or electron-phonon coupling could be accounted for by the QTMC method as well following Eq. (16) provided that appropriate amplitudes for stochastic quantum jumps representing scattering processes are available [43].

We first examine the effect of randomly distributed single vacancies in undoped ($\mu = 0$) graphene driven by a laser with a realistic field strength of 40 kV/cm (Fig. 7). The influence of other short-range defects is expected to be qualitatively similar. We observe a dramatic change of current for individual quantum trajectories, $j_n^m(t)$, calculated for a flake with single vacancies as compared to the disorder-free case. Within each half-cycle of the pulse, the current decreases due to electron backscattering at the vacancies. The total current [Fig. 7(a)] displays a pronounced decrease of its amplitude

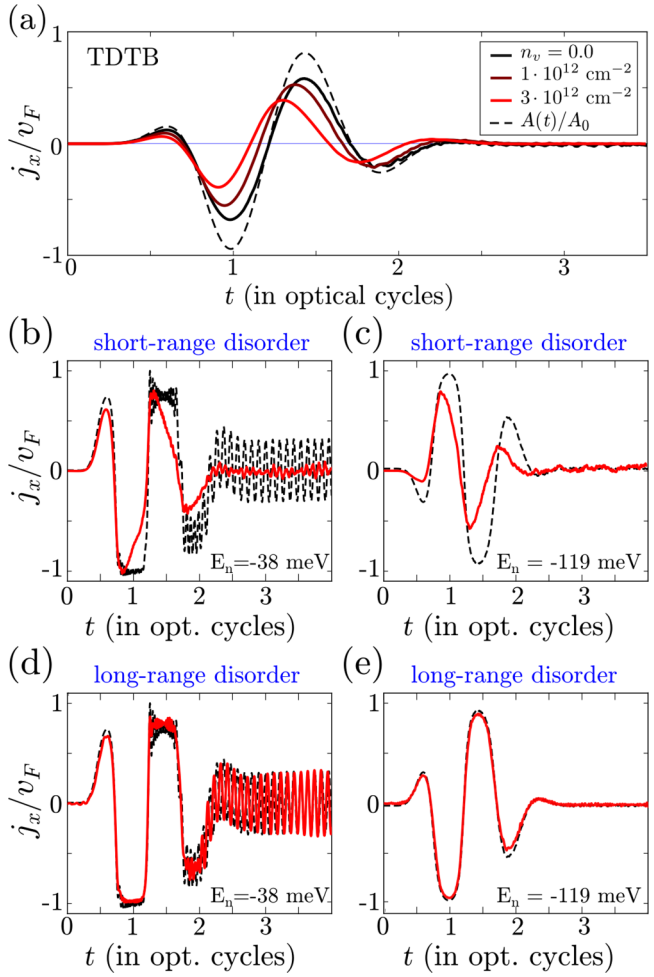

FIG. 7. (a) The total current evaluated within the TDTB approximation for varying density of single vacancies. The black dashed curve is the normalized vector potential of the 2 THz laser pulse with $F_0 = 40$ kV/cm field strength. (b)–(e) Comparison between currents $j_x^n(t)$ of individual quantum trajectories calculated within the TDTB approximation for a $W_x \times W_y = 250 \times 25$ nm^2 flake with periodic boundary conditions in x direction and screened zigzag boundaries parallel to the x axis. Black dashed curves represent $j_x^n(t)$ of an ideal flake and red solid curves represent the corresponding current $j_x^n(t)$ for a flake with (b), (c) randomly distributed single vacancies with density $n_v = 10^{12}$ cm^{-2}; and (d), (e) a smoothly varying random potential with correlation length $l_{\rm cor} = 25$ nm and amplitude $V^{(0)}_{\rm disorder} = 50$ meV. Energy of the initial state in (b), (d) is $E_n = -38$ meV and in (c), (e) is $E_n = -119$ meV.

with increasing amount of disorder due to the enhancement of electron backscattering. Furthermore, in the presence of disorder the response gets out of phase with the vector potential while the current is in phase with $\vec{A}$ for pristine graphene. With increasing disorder density, the current is ahead of the vector potential with increasing phase shift between them. The reason is the decreasing scattering time with increasing disorder. If the scattering time falls below the period of the laser field oscillations (≈500 fs), the disorder backscattering flips the direction of the current before the pulse achieves its maximal vector potential. Including energy loss is expected to lead to a similar phase shift of the current [21].

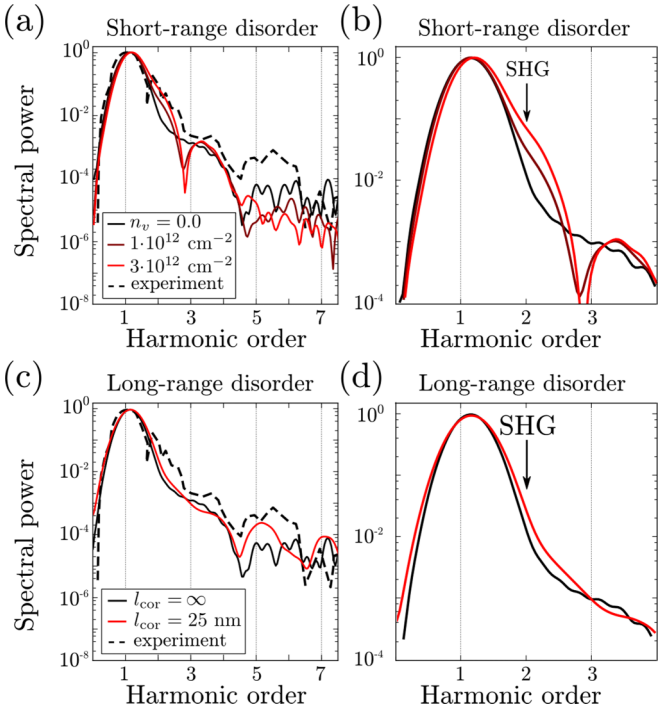

FIG. 8. Power spectrum of the response of undoped graphene flakes to a THz laser pulse with field strength of 40 kV/cm calculated within the TDTB approximation for (a), (b) short- and (c), (d) long-range disorder. (b) and (d) represent zoom-ins of the corresponding spectra in (a) and (c) near the second-order nonlinearity. Black dashed curves are the power spectrum of the measured response [20].

The power spectrum [Eq. (13)] of the total response of the graphene flake in the presence of short-range scatterers [Fig. 8(a)] clearly shows SHG. The intensity of the second-order nonlinearity increases approximately linearly with increasing number of vacancies. By contrast, long-range disorder does not cause the appearance of any significant second-order harmonic component [Fig. 8(b)]. We model long-range disorder as smooth random modulations of the on-site energies with amplitude $V^{(0)}_{\rm disorder} = 50$ meV and a correlation length $l_{\rm cor} = 25$ nm large compared to the lattice constant a_c ($l_{\rm cor}/a_c \gtrsim 100$). This potential describes, for example, charge puddles in graphene on SiO_2 [42]. Estimating a mean-free path for our long-range disorder using a fit to averaged transmission coefficients [48] yields mean-free paths of the order of several micrometers, in line with the reduced backscattering due to pseudospin conservation in graphene. For short-range scattering at vacancies we find much shorter mean-free paths of the order of 100 nm for a vacancy density $n_v = 3 \times 10^{12}/\text{cm}^2$, consistent with the stronger influence of short-range scatterers. Note that for the long-range disorder $l_{\rm cor}$ is still much smaller than the classical quiver amplitude $x_0 = |e|A_0/m\omega = 180$ nm at $F_0 = 40$ kV/cm; i.e., the trajectory fully samples the disorder potential variation. However, long-range disorder does not allow for K-K' (intervalley) scattering, and the intravalley backscattering is weak due to the conservation of chirality for electrons in graphene. Therefore, the second-order response is strongly suppressed as compared to short-range disorder. The latter induces strong intervalley backscattering

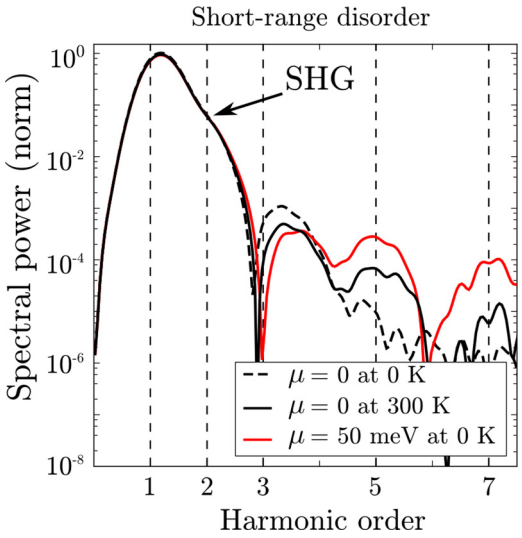

FIG. 9. Power spectrum of the response of graphene flakes with randomly distributed single vacancies with density $n_v = 3 \times 10^{12}$ cm^{-2} calculated within the TDTB approximation for different doping levels and temperature for $F_0 = 40$ kV/cm laser field strength. The response at the doping level of $\mu = 50$ meV and $T = 300$ K (not shown) hardly differs from that at $T = 0$ K presented in the figure.

of electrons [49]. In contrast to single vacancies, long-range disorder does not significantly reduce the current for individual quantum trajectories [Figs. 7(b)–7(e)]. Their envelope still follows that of the currents of the disorder-free case [Figs. 7(d) and 7(e)]. Notably, the interband polarization manifesting itself as oscillations of the current decreases in comparison with the disorder-free case presumably due to the disorder-induced dephasing, i.e., dephasing between the two electron paths moving within the conduction and valence bands.

Allowing for doping by changing the Fermi energy to $\mu = 50$ meV only affects higher order harmonics leaving the intensity of the second-order nonlinearity unchanged (Fig. 9). As we have observed for a disorder-free case (Fig. 6), the harmonics are only slightly modified by finite-temperature effects ($T = 300$ K).

IV. CONCLUSIONS

We have presented a comparative study of the nonlinear response of graphene driven by strong few-cycle THz laser pulses employing (i) the time-dependent Dirac equation for low-energy excitations in bulk graphene and (ii) the time-dependent third-order tight-binding (TDTB) approximation for finite-size graphene flakes. While we find, overall, reasonably good agreement between these complementary methods, the TDTB method allows us to include the effect of disorder scattering on a microscopic level. Taking into account doping changes the nonlinear harmonic intensity due to a decreasing influence of the interband response near the Dirac point. Our analysis demonstrates that short-range disorder allows for second-order harmonic generation (SHG) in graphene due to K-K' scattering. By contrast, long-range disorder does not lead to SHG. The present approach, thus, provides a tool for studying the influence of lattice distortions, vacancies, adatoms in graphene, as well as charge puddles and moiré effects due to a substrate on the nonlinear response of graphene. Our calculations agree well with a recent experiment where the second, third, and fifth harmonics were observed in multilayer epitaxial graphene [20].

ACKNOWLEDGMENTS

We gratefully acknowledge support from the Austrian Fonds zur Förderung der wissenschaftlichen Forschung (FWF) through the FWF-SFB 041-ViCom, FWF-SFB 049-NextLite, and FWF doctoral college Solids4Fun (W1243). Calculations were performed on the Vienna Scientific Cluster.

[1] D. Golde, T. Meier, and S. W. Koch, Phys. Rev. B **77**, 075330 (2008).
[2] S. Ghimire, A. D. DiChiara, E. Sistrunk, P. Agostini, and L. F. DiMauro, Nat. Phys. **7**, 138 (2011).
[3] G. Vampa, T. J. Hammond, N. Thiré, B. E. Schmidt, F. Légaré, C. R. McDonald, T. Brabec, and P. B. Corkum, Nature (London) **522**, 462 (2015).
[4] T. T. Luu, M. Garg, S. Yu. Kruchinin, A. Moulet, M. Th. Hassan, and E. Goulielmakis, Nature (London) **521**, 498 (2015).
[5] O. Schubert, M. Hohenleutner, F. Langer, B. Urbanek, C. Lange, U. Huttner, D. Golde, T. Meier, M. Kira, S. W. Koch, and R. Huber, Nat. Photonics **8**, 119 (2014).
[6] M. Hohenleutner, F. Langer, O. Schubert, M. Knorr, U. Huttner, S. W. Koch, M. Kira, and R. Huber, Nature (London) **523**, 572 (2015).
[7] G. Wachter, C. Lemell, J. Burgdörfer, S. A. Sato, X.-M. Tong, and K. Yabana, Phys. Rev. Lett. **113**, 087401 (2014).
[8] M. Krüger, M. Schenk, and P. Hommelhoff, Nature (London) **475**, 78 (2011).
[9] A. V. Mitrofanov, A. J. Verhoef, E. E. Serebryannikov, J. Lumeau, L. Glebov, A. M. Zheltikov, and A. Baltuška, Phys. Rev. Lett. **106**, 147401 (2011).
[10] G. Vampa, T. J. Hammond, N. Thiré, B. E. Schmidt, F. Légaré, C. R. McDonald, T. Brabec, D. D. Klug, and P. B. Corkum, Phys. Rev. Lett. **115**, 193603 (2015).
[11] K. Krieger, J. K. Dewhurst, P. Elliott, S. Sharma, and E. K. U. Gross, J. Chem. Theor. Comput. **11**, 4870 (2015).
[12] P. Elliott, K. Krieger, J. K. Dewhurst, S. Sharma, and E. K. U. Gross, New J. Phys. **18**, 013014 (2016).
[13] M. M. Glazov and S. D. Ganichev, Phys. Rep. **535**, 101 (2013).
[14] Anton Y. Bykov, Tatiana V. Murzina, Maxim G. Rybin, and Elena D. Obraztsova, Phys. Rev. B **85**, 121413(R) (2012).
[15] E. Hendry, P. J. Hale, J. Moger, A. K. Savchenko, and S. A. Mikhailov, Phys. Rev. Lett. **105**, 097401 (2010).

[16] J. Maysonnave, S. Huppert, F. Wang, S. Maero, C. Berger, W. de Heer, T. B. Norris, L. A. De Vaulchier, S. Dhillon, J. Tignon, R. Ferreira, and J. Mangeney, Nano Lett. **14**, 5797 (2014).
[17] H. A. Hafez, I. Al-Naib, M. M. Dignam, Y. Sekine, K. Oguri, F. Blanchard, D. G. Cooke, S. Tanaka, F. Komori, H. Hibino, and T. Ozaki, Phys. Rev. B **91**, 035422 (2015).
[18] L. Prechtel, L. Song, D. Schuh, P. Ajayan, W. Wegscheider, and A. W. Holleitner, Nat. Commun. **3**, 646 (2012).
[19] M. J. Paul, Y. C. Chang, Z. J. Thompson, A. Stickel, J. Wardini, H. Choi, E. D. Minot, B. Hou, J. A. Nees, T. B. Norris, and Y.-S. Lee, New J. Phys. **15**, 085019 (2013).
[20] P. Bowlan, E. Martinez-Moreno, K. Reimann, T. Elsaesser, and M. Woerner, Phys. Rev. B **89**, 041408(R) (2014).
[21] S. A. Mikhailov and K. Ziegler, J. Phys.: Condens. Matter **20**, 384204 (2008).
[22] K. L. Ishikawa, Phys. Rev. B **82**, 201402(R) (2010).
[23] I. Al-Naib, J. E. Sipe, and M. M. Dignam, Phys. Rev. B **90**, 245423 (2014).
[24] I. Al-Naib, M. Poschmann, and M. M. Dignam, Phys. Rev. B **91**, 205407 (2015).
[25] L. A. Chizhova, F. Libisch, and J. Burgdörfer, Phys. Rev. B **90**, 165404 (2014).
[26] S. Reich, J. Maultzsch, C. Thomsen, and P. Ordejón, Phys. Rev. B **66**, 035412 (2002).
[27] K. Kristinsson, O. V. Kibis, S. Morina, and I. A. Shelykh, Sci. Rep. **6**, 20082 (2016).
[28] J. C. W. Song, K. J. Tielrooij, F. H. L. Koppens, and L. S. Levitov, Phys. Rev. B **87**, 155429 (2013).
[29] K. J. Tielrooij, J. C. W. Song, S. A. Jensen, A. Centeno, A. Pesquera, A. Z. Elorza, M. Bonn, L. S. Levitov, and F. H. L. Koppens, Nat. Phys. **9**, 248 (2013).
[30] K. L. Ishikawa, New J. Phys. **15**, 055021 (2013).
[31] G. Kaiser, *A Friendly Guide to Wavelets*, Modern Birkhäuser Classics (Birkhäuser, Boston, 2011).
[32] C. Zener, Proc. R. Soc. London A **145**, 523 (1934).
[33] Z.-G. Chen, Z. Shi, W. Yang, X. Lu, Y. Lai, H. Yan, F. Wang, G. Zhang, and Z. Li, Nat. Commun. **5**, 4461 (2014).
[34] D. J. Tannor, *Introduction to Quantum Mechanics* (University Science Books, Sausalito, CA, 2007).
[35] R. E. Peierls, Z. Phys. **80**, 763 (1933).
[36] S. I. Simonsen, S. A. Sørngård, M. Førre, and J. P. Hansen, J. Phys. B **47**, 065401 (2014).
[37] K. Yabana, T. Sugiyama, Y. Shinohara, T. Otobe, and G. F. Bertsch, Phys. Rev. B **85**, 045134 (2012).
[38] C. Aversa and J. E. Sipe, Phys. Rev. B **52**, 14636 (1995).
[39] M. V. Berry and R. J. Mondragon, Proc. R. Soc. London A **412**, 53 (1987).
[40] G. Wachter, S. A. Sato, I. Floss, C. Lemell, X.-M. Tong, K. Yabana, and J. Burgdörfer, New J. Phys. **17**, 123026 (2015).
[41] F. Banhart, J. Kotakoski, and A. V. Krasheninnikov, ACS Nano **5**, 26 (2011).
[42] J. Martin, N. Akerman, G. Ulbricht, T. Lohmann, J. H. Smet, K. von Klitzing, and A. Yacoby, Nat. Phys. **4**, 144 (2007).
[43] M. Seliger, C. O. Reinhold, T. Minami, and J. Burgdörfer, Phys. Rev. A **71**, 062901 (2005).
[44] P. Bowlan, E. Martinez-Moreno, K. Reimann, M. Woerner, and T. Elsaesser, New J. Phys. **16**, 013027 (2014).
[45] J. M. Iglesias, M. J. Martin, E. Pascual, and R. Rengel, J. Phys.: Conf. Ser. **647**, 012003 (2015).
[46] M. T. Mihnev, J. R. Tolsma, C. J. Divin, D. Sun, R. Asgari, M. Polini, C. Berger, W. A. de Heer, A. H. MacDonald, and T. B. Norris, Nat. Commun. **6**, 8105 (2015).
[47] F. Kadi, T. Winzer, E. Malic, A. Knorr, F. Göttfert, M. Mittendorff, S. Winnerl, and M. Helm, Phys. Rev. Lett. **113**, 035502 (2014).
[48] J. Doppler, J. A. Méndez-Bermúdez, J. Feist, O. Dietz, D. O. Krimer, N. M. Makarov, F. M. Izrailev, and S. Rotter, New J. Phys. **16**, 053026 (2013).
[49] F. Libisch, S. Rotter, and J. Burgdörfer, Phys. Status Solidi B **248**, 2598 (2011). F. Libisch, A. Klimann, S. Rotter, and J. Burgdörfer, Phys. Status Solidi B, doi:10.100/pssb.201600260 (2016).